Impact of Configurations of Rapid Intermittent Assimilation of WSR-88D Radar Data for the 8 May 2003 Oklahoma City Tornadic Thunderstorm Case

MING HU AND MING XUE

Center for Analysis and Prediction of Storms, and School of Meteorology, University of Oklahoma, Norman, Oklahoma

ABSTRACT

Various configurations of the intermittent data assimilation procedure for Level-II Weather Surveillance Radar-1988 Doppler radar data are examined for the analysis and prediction of a tornadic thunderstorm that occurred on 8 May 2003 near Oklahoma City, Oklahoma. Several tornadoes were produced by this thunderstorm, causing extensive damages in the south Oklahoma City area. Within the rapidly cycled assimilation system, the Advanced Regional Prediction System three-dimensional variational data assimilation (ARPS 3DVAR) is employed to analyze conventional and radar radial velocity data, while the ARPS complex cloud analysis procedure is used to analyze cloud and hydrometeor fields and adjust in-cloud temperature and moisture fields based on reflectivity observations and the preliminary analysis of the atmosphere. Forecasts for up to 2.5 h are made from the assimilated initial conditions. Two one-way nested grids at 9- and 3-km grid spacings are employed although the assimilation configuration experiments are conducted for the 3-km grid only while keeping the 9-km grid configuration the same. Data from the Oklahoma City radar are used. Different combinations of the assimilation frequency, in-cloud temperature adjustment schemes, and the length and coverage of the assimilation window are tested, and the results are discussed with respect to the length and evolution stage of the thunderstorm life cycle. It is found that even though the general assimilation method remains the same, the assimilation settings can significantly impact the results of assimilation and the subsequent forecast. For this case, a 1-h-long assimilation window covering the entire initial stage of the storm together with a 10-min spinup period before storm initiation works best. Assimilation frequency and in-cloud temperature adjustment scheme should be set carefully to add suitable amounts of potential energy during assimilation. High assimilation frequency does not necessarily lead to a better result because of the significant adjustment during the initial forecast period. When a short assimilation window is used, covering the later part of the initial stage of storm and using a high assimilation frequency and a temperature adjustment scheme based on latent heat release can quickly build up the storm and produce a reasonable analysis and forecast. The results also show that when the data from a single Doppler radar are assimilated with properly chosen assimilation configurations, the model is able to predict the evolution of the 8 May 2003 Oklahoma City tornadic thunderstorm well for up to 2.5 h. The implications of the choices of assimilation settings for real-time applications are discussed.

1. Introduction

The operational Weather Surveillance Radar-1988 Doppler (WSR-88D) radar network of the United States (Crum and Alberty 1993) has dramatically improved the ability of severe weather warning in routine operations (Serafin and Wilson 2000); it is also playing an important role in storm-scale data assimilation and

model initialization because it is the only observational network that can resolve convective storms. However, creating a complete set of initial conditions for numerical weather prediction (NWP) using radar data is challenging because radars only observe a very limited set of parameters, mainly the radial velocity and reflectivity. Further, their spatial coverage is usually incomplete. To build up dynamically consistent storms in a model from radar observations, a retrieval or assimilation method that takes advantage of the high data frequency is usually necessary.

The four-dimensional variational data assimilation (4DVAR) method is considered ideal for this purpose,

Corresponding author address: Dr. Ming Xue, Center for Analysis and Prediction of Storms, National Weather Center, Suite 2500, 120 David L. Boren Blvd., Norman, OK 73072.
E-mail: mxue@ou.edu

and some encouraging results with both simulated and real radar data have been obtained (Sun et al. 1991; Sun and Crook 1997, 1998; Sun 2005). However, the difficulty of getting the adjoint code and the high cost of computation are limiting its use in research and operation. Another relatively new technique is the ensemble Kalman filter (EnKF) data assimilation, which can produce a quality assimilation of thunderstorms similar to the 4DVAR when tested with simulated single-Doppler radar data (Snyder and Zhang 2003; Zhang et al. 2004; Tong and Xue 2005; Xue et al. 2006). While also expensive in computation, the EnKF method is easier to implement and more flexible because no complex adjoint code is needed and the algorithm can be rather simple.

Other simpler and faster methods retrieve unobserved wind components (Qiu and Xu 1992, 1994; Xu et al. 1994; Shapiro et al. 1995; Gao et al. 2001) and then thermodynamic fields from the analyzed winds (Gal-Chen 1978). The retrieved fields can then be analyzed into model initial conditions (Weygandt et al. 2002a,b). The quality of retrieved thermodynamic fields heavily depends on the quality of the wind retrievals and the frequency of the wind fields.

Another efficient way to assimilate multiple radar volume scans is to employ intermittent assimilation cycles with fast analysis methods, such as the three-dimensional variational data assimilation (3DVAR), Advanced Regional Prediction System (ARPS; Xue et al. 1995, 2000, 2001) Data Analysis System (ADAS; Brewster 1996), and the APRS complex cloud analysis. The intermittent data assimilation treats the data observed around a certain analysis time as valid at that particular time and assimilates the data into the model periodically (Daley 1991). The ARPS 3DVAR (Gao et al. 2002, 2004) can analyze the radar radial velocity data and other conventional data variationally, while the ADAS uses the Bratseth (1986) scheme to analyze conventional observations and a simple procedure to adjust wind from radial velocity. The cloud analysis procedure retrieves thermodynamic and microphysical fields from the reflectivity according to semiempirical rules (Zhang et al. 1998; Zhang 1999) and can be used with both the ARPS 3DVAR and ADAS. A similar procedure was also employed in the Local Analysis and Prediction System (LAPS; Albers et al. 1996).

Recently, Hu et al. (2006a,b) demonstrated for a cluster of thunderstorms that occurred on 28 March 2000 in Fort Worth, Texas, that the ARPS 3DVAR and the ARPS cloud analysis together, through intermittent assimilation cycles at 10-min intervals over a 1-h-long window, are able to successfully build up dynamically consistent storms in the model. Starting from such an initial condition, the ARPS model is able to predict individual storm cells with reasonable accuracy for up to 2 h. The prediction captured the supercell characteristics of the storm that spawned two individual tornadoes. An in-cloud temperature adjustment scheme based on the moist adiabat associated with a lifted low-level parcel is used in their control experiment.

In this study, the above assimilation and forecast system is applied to a new case, the 8 May 2003 Oklahoma City, Oklahoma (OKC), tornadic thunderstorm. Data from the Oklahoma City WSR-88D radar (KTLX) are assimilated. Again using a nested grid at 3-km horizontal resolution, the ARPS model is able to predict many aspects of the propagation and supercell characteristics of the OKC storm for up to 2.5 h. It is found, however, that the results of assimilation and prediction are sensitive to the details of the assimilation configurations. The assimilation frequency, the in-cloud temperature adjustment scheme used, and the length and coverage of the assimilation window (AW) all affect the results. It is the goal of this study to investigate how these different configurations affect the results and why. In addition, this study serves to document the application of our 3DVAR and cloud analysis procedure to another tornadic supercell case. This case differs from the Fort Worth case in that the main thunderstorm was more isolated and lasted for a longer period of time.

The organization of this paper is as follows: In section 2, the 8 May Oklahoma City tornadic thunderstorm case is described. In section 3, we introduce the design of a set of experiments for studying the impact of the assimilation configurations. A detailed comparison among experiments is presented in section 4, and the results are further discussed and summarized in section 5.

2. The 8 May 2003 Oklahoma City tornadic thunderstorm case

At about 2210 UTC [1610 local standard time (LST)] 8 May 2003, Moore, a suburban city about 15 km south of Oklahoma City, was struck by a major tornado for the fourth time in 5 yr. The tornado tracked east-northeast for about 30 km on the ground, from Moore to Choctaw, Oklahoma, and dissipated at 2238 UTC (Fig. 1). It caused large areas of F3 (on Fujita scale of tornado intensity) and small areas of F4 damages south and east of OKC and many F2 damages in the Moore area. This tornado produced $370 million worth of damages and more than 100 injuries but fortunately no deaths. It is named the OKC tornado by the
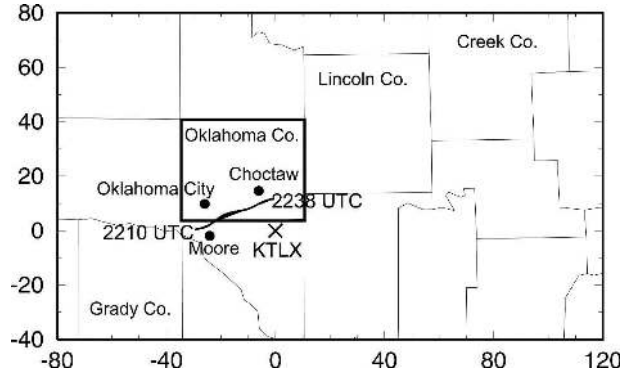
FIG. 1. Map of counties and cities related to the 8 May 2003 OKC tornadic thunderstorm. The dark line segment starting at 2210 UTC northwest of Moore and ending at 2238 UTC south Choctaw marks roughly the damage path of the main OKC tornado, which was the third tornado from the OKC thunderstorm (two other tornados from this storm were much weaker and had not recorded damage paths). The x and y distances are in kilometers and are relative to the KTLX radar marked by a times sign in the figure. Oklahoma County is highlighted.

FIG. 2. Regions of radar echoes exceeding 35 dBZ as observed by the KTLX radar at the 1.45° elevation. The echoes are at 30-min intervals from 2101 to 2359 UTC 8 May 2003. The gray-scales of the echoes at two consecutive times are different; so are their outlines. The locations of the maximum reflectivity of the main storm are marked by plus signs together with the corresponding times. The x and y coordinates are in kilometers and originate at the KTLX radar site that is marked by a times sign. The arrow lines are the trajectories of the OKC storm and storms A, B, and C. Also, the hook echo at 2201 UTC and Moore, OK, are pointed out by curved arrows. Oklahoma County is highlighted.

National Weather Service, as it struck the general OKC area. The parental storm is referred to as the OKC tornadic thunderstorm.

Two additional short-lived tornadoes from the same storm were reported near Moore. The first brief tornado occurred at 2200 UTC. The second F0 tornado began at 2204 UTC, stayed on the ground, and moved nearly 3 km in 6 min but dissipated just before the OKC tornado outbreak.

On 8 May 2003, the synoptic-scale environment over Oklahoma was favorable for tornadic thunderstorms. A surface low formed in the early morning in southeastern Colorado and propagated northeastward across Kansas during the daytime. Oklahoma and Texas had been exposed to southerly flows for all day and a north–south-oriented dryline formed over western Texas and the Texas–Oklahoma Panhandle area by 1200 UTC (0600 LST). The dryline then moved eastward into western Oklahoma and by 1800 UTC (1200 LST) it was located about 200 km west of OKC. During the daytime, the upper-level flows over Oklahoma were mainly southwesterlies, with the wind speed slightly increasing before the thunderstorms.

The 1800 UTC 8 May Norman, Oklahoma (OUN), sounding shows a large instability with a 4004 J kg^{-1} convective available potential energy (CAPE) and a 1 J kg^{-1} convective inhibition (CIN). The vertical shear of horizontal winds over the lowest 6 km is about 25 m s^{-1}. These conditions suggest a strong potential for supercell storms or even tornados.

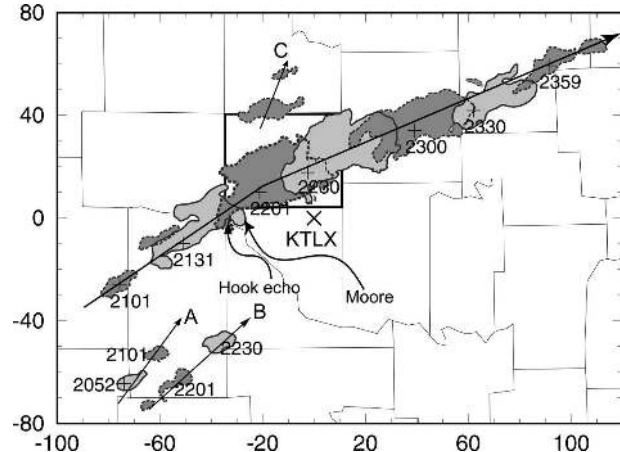At 2040 UTC, the OKC tornadic thunderstorm was initiated east of the dryline, observed as a weak echo by the KTLX radar. The evolution of the storm is displayed by a series of low-level reflectivity regions whose values are greater than 35 dBZ (Fig. 2). The storm developed into a strong cell by 2101 UTC and was located at $(-75, -27)$ km relative to the KTLX radar. It then propagated northeastward and grew significantly in size over the next hour. At 2201 UTC, a pronounced hook appendage structure was found at the southwestern end of the storm, northwest of Moore, indicating the presence of a tornado or mesocyclone. The supercell storm propagated east-northeastward, then became weaker at 2300 UTC 8 May, and dissipated by 0020 UTC 9 May. In addition to the OKC storm, three other storms are also shown in Fig. 2 and are referred to as storms A, B, and C. Storm A was initiated a little earlier than the OKC storm east of the dryline but dissipated by 2130 UTC. Storm B was initiated later than the OKC storm and lasted for only about 1 h. Storm C was split from the OKC storm and dissipated quickly during its leftward propagation.

3. Design of assimilation and forecast experiments

In this paper, data from the KTLX radar are assimilated to study the impact of different assimilation configurations on the initialization and prediction of the OKC storm. The low-level reflectivity observations from the same radar are used to evaluate the quality of

the forecasts, which are available at high enough temporal and spatial resolutions for resolving the storm. Radial velocity data are also used (but to a less extent) for forecast verification.

For all experiments, two one-way nested grids with 9- and 3-km horizontal resolutions, respectively, are used. The 9-km grid covers an area of 2300 km × 2300 km with Oklahoma located roughly at the center. The 3-km grid is 580 km × 580 km in size and covers the entire state of Oklahoma and parts of Texas and Kansas. Both the 9-km and 3-km simulations use the same vertical grid, which has 53 layers and stretches from about 20 m at the surface to 770 m at the model top that is located at 21.1-km height. The ARPS model with full physics is used during the assimilation and in the forecast. The ARPS 3DVAR is used to analyze wind profilers, routine surface observations, Oklahoma Mesonet data (Brock et al. 1995), and radar radial velocity data while the cloud analysis procedure is used to analyze reflectivity data.

The ARPS 3DVAR uses an incremental form of the cost function that includes the background, observation, and equation constraint terms. The analysis variables include the three wind components, potential temperature, pressure, and water vapor mixing ratio (Gao et al. 2004). In the current system, the cross correlations between variables are not included in the background error covariance. The spatial covariances of background error are modeled using a recursive filter. The observation errors are assumed to be uncorrelated. Multiple analysis passes are used to analyze different data types with different filter scales, with the filter scales chosen mainly according to the density of the observational network to which the filter is applied.

The cloud analysis procedure can incorporate cloud reports from surface observations, standard aviation routine weather reports, geostationary satellite infrared and visible imagery data, and radar reflectivity data to construct three-dimensional cloud and precipitation fields. The in-cloud temperature is also adjusted to be consistent with the cloud fields. To isolate the impact of radar data, only reflectivity data are used by the cloud analysis in this study. Additional details on the applications of the ARPS 3DVAR and cloud analysis to the initialization of convective storms can be found in Hu et al. (2006a,b).

Only one 9-km experiment is conducted and its forecasts at different times provide the background for the first 3-km analysis and the boundary conditions for 3-km assimilation and forecast. The 9-km experiment includes 1-h assimilation cycles over a 6-h period from 1800 UTC 8 May to 0000 UTC 9 May. The 9-km analysis uses the NCEP Eta Model 1800 UTC analysis as the

background and the analysis includes only rawinsonde and wind profiler data. A special OUN sounding at 1800 UTC is included. The lateral boundaries are forced by the Eta 1800 UTC forecasts at 3-h intervals.

Before being used in the 3-km analysis, the observed KTLX reflectivity and radial velocity data first pass through the ADAS quality control procedure, which includes velocity dealiasing, clutter removal, etc. The quality controlled data then pass through visual inspections, and further minor corrections and adjustments are made. The data are then remapped from the radar coordinates to the model grid columns for use by the ARPS 3DVAR and the cloud analysis.

The 3-km control experiment starts at 2030 UTC—slightly earlier than the initiation time of the OKC storm. The 1-h-long assimilation window with 10-min intervals covers the entire initiation stage of the storm. Both reflectivity and radial velocity data are assimilated along with the upper-air data when available. The two-pass strategy with different decorrelation scales for each pass is used in the 3DVAR. The upper-air data are analyzed in the first pass using a horizontal decorrelation scale length of 120 km and the radar radial velocity data are analyzed in the second pass using a scale length of 6 km. For the 3-km control experiment, a 2.5-h forecast is conducted from the end result of assimilation at 2130 UTC—40 min before the storm produced the OKC tornado northwest of Moore.

Based on the control experiment, a series of other 3-km experiments are conducted, using different assimilation configurations to study their impacts on the assimilation and subsequent forecast. The configuration parameters that are varied include assimilation frequencies (or intervals), in-cloud temperature adjustment schemes, and the lengths and coverage of AW.

A total of thirteen 3-km experiments (Table 1) are conducted, including the control. These experiments can be classified into two groups according to assimilation frequency, that is, the experiments with 5- or 10-min analysis cycles. In each group, the length of the AW varies from 30 to 60 min and the AW covers different stages of the OKC storm development. The latter include the entire initiation stage (from 2030 to 2130 UTC), the early stage of initiation (from 2030 to 2110 or 2120 UTC), and the late stage of initiation (from 2040 or 2060 to 2130 UTC). For in-cloud temperature adjustment, two schemes are available in the ARPS cloud analysis package. One is based on the latent heat release (Zhang et al. 1998; referred to as the LH scheme) associated with the cloud condensate amount, and the other is based on a moist adiabatic temperature profile (Brewster 2002; referred to as the MA scheme). All experiments with 5-min intervals use the MA scheme

TABLE 1. Assimilation configurations of the 3-km experiments.

Name[a]	Interval (min)	Length (min)	Coverage (UTC)[b]	In-cloud temperature adjustment[c]	ETS at 1.5-h forecast
10B30E30LH (CNTL)	10	60	2030–2130	LH	0.473
5B30E30MA	5	60	2030–2130	MA	0.292
10B30E30MA	10	60	2030–2130	MA	0.174
5B30E30LH	5	60	2030–2130	LH	0.0
10B30E20LH	10	50	2030–2120	LH	0.359
10B30E10LH	10	50	2030–2110	LH	0.013
5B30E20MA	5	50	2030–2120	MA	0.027
5B30E10MA	5	40	2030–2110	MA	0.0
10B40E30LH	10	50	2040–2130	LH	0.320
10B60E30LH	10	30	2100–2130	LH	0.044
5B40E30MA	5	50	2040–2130	MA	0.194
5B60E30MA	5	30	2100–2130	MA	0.0
5B60E30LH	5	30	2100–2130	LH	0.372

[a] Characters B and E followed by a number denote, respectively, the beginning and ending time of the AW in minutes out of the hour.
[b] Experiments whose AW starts at 2130 UTC have a 10-min spinup time prior to the first volume scan of precipitation-mode radar data.
[c] LH refers to the latent heat–based scheme that calculates the temperature adjustment from the latent heat release, and MA refers to the moist adiabat–based scheme that adjusts in-cloud temperature using a boundary layer–based moist adiabat.

except for experiments 5B30E30LH and 5B60E30LH, which use the LH scheme. All experiments with 10-min analysis intervals use the LH scheme except for experiment 10B30E30MA, which uses the MA scheme. The details of the two temperature adjustment schemes and the ideal combination of one of them with other configuration parameters are discussed in the next section.

4. The results of assimilation and forecast experiments

In this section, we first discuss the results of control experiment 10B30E30LH (also called CNTL), which produced the best forecast (judged in terms of the propagation and evolution of the main OKC storm) among the 13 experiments. The experiments with different assimilation frequencies, in-cloud temperature adjustment schemes, and assimilation lengths and coverage are then discussed and compared. Finally, the results of experiment 5B60E30LH, in which the assimilation configurations are adjusted to suit a shorter AW, are discussed.

a. The experiment with the best forecast

The experiment that produces the best forecast, that is, control experiment 10B30E30LH, employs a 1-h-long AW from 2030 to 2130 UTC with 10-min analysis cycles (about every other radar volume scan). The LH scheme is used for in-cloud temperature adjustment (Table 1). As mentioned before, the first echo of the

OKC storm appeared at 2040 UTC and the first tornado from the storm occurred at 2200 UTC. The AW of this experiment, therefore, covers the entire initial development stage of the storm and the final analysis has a half-hour lead time from the tornadogenesis stage of the storm.

A sounding extracted from the 2030 UTC analysis of the 3-km control experiment near the OUN station has a 3513 J kg^{-1} CAPE and a 0 J kg^{-1} CIN. Its vertical shear of horizontal winds over the lowest 6 km is about 32 m s^{-1}. Compared to the observed 1800 UTC OUN sounding described earlier, the model environment at this time has less instability but more vertical shear and remains favorable for supercell storms.

The regions with reflectivity exceeding 45 dBZ, as observed by the OKC KTLX radar at the 1.45° elevation, are shown in Fig. 3 together with the corresponding predicted reflectivity fields from 10B30E30LH. The time period shown in Fig. 3 is from 2130 UTC 8 May to 0000 UTC 9 May. The observed storm first formed at the northeast corner of Grady County (cf. Fig. 1), propagated east-northeastward through Oklahoma and Lincoln Counties, and arrived at east-central Creek County 2.5 h later (Fig. 3a). Experiment 10B30E30LH predicts the observed storm motion accurately (Fig. 3b); the predicted storm moves in essentially the same direction and at about the same speed as the observed storm. The location errors of the maximum reflectivity of the predicted OKC storm are within 8 km in the entire 2.5 h of forecast. The observed storm grew
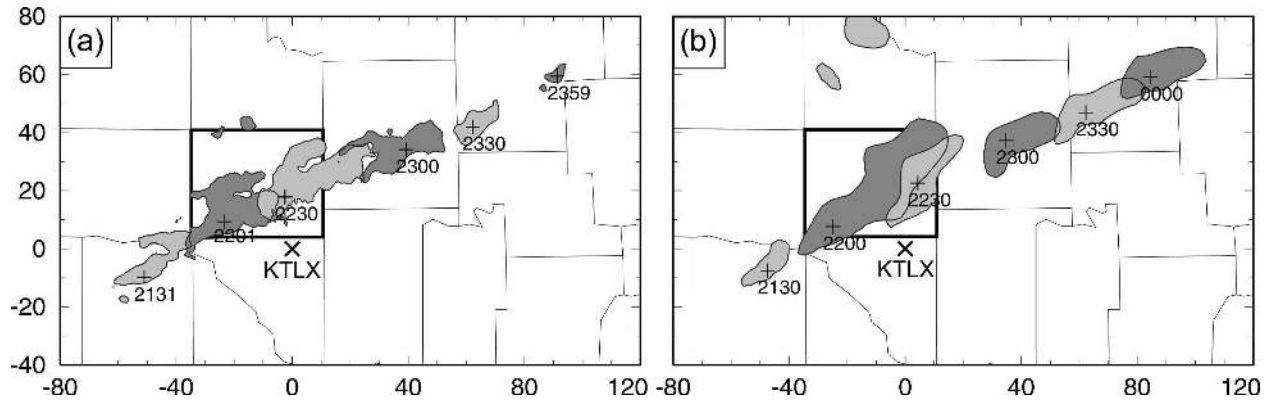
FIG. 3. As in Fig. 2, but for (a) the observations from 2130 UTC 8 May to 0000 UTC 9 May 2003 at 30-min intervals and (b) the corresponding analyzed (at 2130 UTC) and predicted reflectivity fields from experiment 10B30E30LH. Regions with reflectivity exceeding 45 dB*Z* are shown. The locations of the maximum reflectivity of the OKC storm are marked by plus signs together with the corresponding times. The domain shown represents the portion of the 3-km grid between 210 and 410 km in the east–west direction and between 260 and 380 km in the north–south direction.

quickly from 2131 to 2201 UTC, then remained as a supercell with a large area of strong reflectivity (>45 dB*Z*; shown as shaded regions in Fig. 3) until 2300 UTC. A pronounced hook echo existed at the southwest end of the high-reflectivity region between 2201 and 2300 UTC. After 2300 UTC, the storm weakened, and by 2359 UTC only a small area of high reflectivity (>45 dB*Z*) remained. The main characteristics of the development of the observed storm are also captured by the forecast; the predicted storm reaches its maximum intensity at about 2200 UTC but misses the start of the dissipating stage at 2300 UTC. Overall, 10B30E30LH successfully predicts the development and propagation of the OKC thunderstorm even though it is somewhat too strong in the last hour of the forecast.

The predicted reflectivity fields at 1.45° elevation at 2200 and 2300 UTC from 10B30E30LH are shown in more detail in Figs. 4b,d, together with the corresponding observations (Figs. 4a,c). At 2200 UTC, the time when the OKC storm produced the first tornado, a clear hook echo is seen at the southwest (SW) end of the observed storm (Fig. 4a) and two small left-moving cells are seen north of the storm. The half-hour forecast of 10B30E30LH at this time produces the right position and reflectivity intensity of the storm, but does not exhibit a clear hook shape at the SW end (Fig. 4b). One hour later, the observed storm remained strong and moved to central Lincoln County (Fig. 4c). Although the OKC tornado ended about 20 min earlier, the storm still possesses a strong reflectivity gradient and hook-shaped echo at its south flank, indicating its supercell characteristics. Again, the 1.5-h forecast of 10B30E30LH at 2300 UTC gives an accurate position and reflectivity intensity of the storm (Fig. 4d); as observed, the pre-

dicted storm also exhibits supercell characteristics—a hook-shaped echo with a strong reflectivity gradient at its south flank.

To further evaluate the prediction in terms of the wind field, the predicted radial velocity fields at 1.45° elevation at 2210 and 2225 UTC from 10B30E30LH are plotted in Figs. 5b,d together with the corresponding observations (Figs. 5a,c). At 2210 UTC, the beginning time of the OKC tornado, a strong radial velocity couplet located near the southwest end of the tornado damage path is found in the radial velocity observations (Figs. 5a, 1). The 40-min forecast valid at the same time also shows a cyclonic radial velocity couplet, but the feature is much weaker and is displaced northeastward by about 15 km. Fifteen minutes later, the observed tornado became stronger and its related radial velocity couplet also intensified and moves along the damage path toward the east (Fig. 5c). The cyclonic couplet in predicted radial velocity fields also moves eastward but becomes weaker and elongated in shape (Fig. 5d). Despite the differences in details, the model prediction does contain clear features of low-level rotation. The general structure and evolution of the predicted storm in control experiment 10B30E30LH can be considered good, especially given the relatively low resolution.

b. The impact of the frequency of analysis cycles

In the control experiment, the KTLX radar data are used every 10 min, while the volume scan interval of operational WSR-88D radars (such as KTLX) operating in the precipitation mode is about 5 min. To study the impact of the frequency of analysis cycles on the prediction of storms, experiment 5B30E30MA is conducted. This experiment is the same as the control ex-
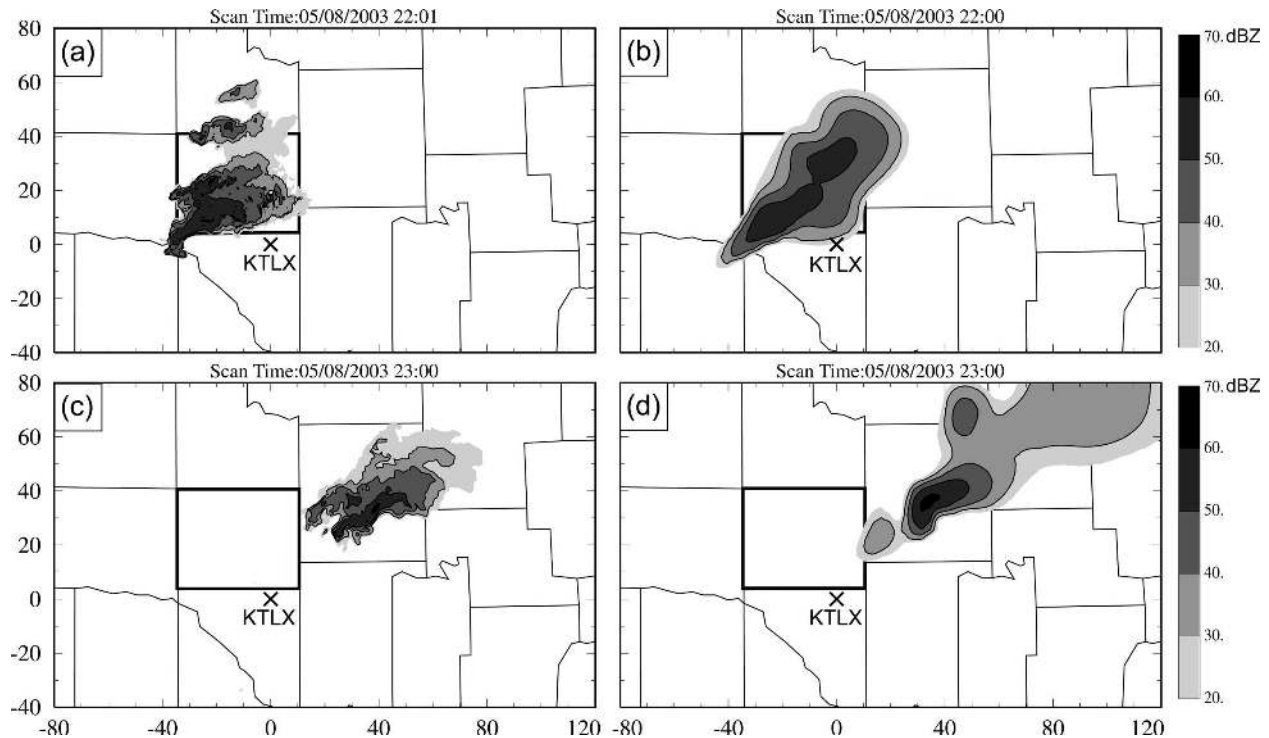
FIG. 4. Observed reflectivity fields at the (a), (c) 1.45° elevation of the KTLX radar and (b), (d) corresponding predicted reflectivity from experiment 10B30E30LH at 2200 UTC (30-min forecast time) and 2300 UTC (1.5-h forecast time) 8 May 2003. The reflectivity contours are at 30, 40, 50, and 60 dBZ. The domain shown is the same as Fig. 3.

cept for its 5-min analysis cycles and the use of an MA scheme for in-cloud temperature adjustment (Table 1). The reason for using a different in-cloud temperature adjustment scheme is discussed in the next subsection.

The regions with predicted reflectivity exceeding 45 dBZ at the 1.45° elevation are shown in Fig. 6 for experiment 5B30E30MA every 30 min. Compared to the observations (Fig. 3a), 5B30E30MA predicts the motion of the OKC storm very well but gives a wrong trend of storm evolution. Contrary to the observations, the predicted storm becomes weaker from 2200 to 2300 UTC and then stronger from 2300 UTC on. The positions of the predicted maximum reflectivity in 10B30E30LH are better than those in 5B30E30MA most of the time (Figs. 3b, 6), and the evolution of the storm strength (judging by the size of the large reflectivity region) is better captured by 10B30E30LH too, even though 10B30E30LH overpredicts the intensity of the storm at the dissipation stage.

To quantitatively compare the quality of the forecasts from 10B30E30LH and 5B30E30MA, equitable threat scores (ETSs; Schaefer 1990) of the predicted reflectivity at the 1.45° elevation for the 45-dBZ threshold are calculated against the observations and plotted in Fig. 7. The ETS is originally designed for large-scale

precipitation prediction and should be applied with caution for small-scale convection systems. ETS here is used in a similar way as we do in Hu et al. (2006a). Figure 7 shows that the first-hour forecasts (from 2130 to 2230 UTC, 8 May) of the two experiments are similar except for 0.75 h, when 5B30E30MA is better. For the next 1.5 h, 10B30E30LH has much higher scores than 5B30E30MA. The largest difference occurs at 1.5 h (2300 UTC), when the scores for 10B30E30LH and 5B30E30MA are 0.48 and 0.29, respectively. This is the time when the storm in 5B30E30MA is too weak (Fig. 6). The comparisons of ETSs for these two experiments agree with the earlier subjective evaluation.

Usually, the data assimilation that uses more observations is expected to produce initial conditions that lead to better forecasts, but both subjective evaluation and the ETS for the previous two experiments suggest that the experiment with lower assimilation frequency (10-min intervals) gives a better forecast. The reason is complex and appears to be related to both the ability of the analysis procedure to generate storms with a dynamically consistent state in the initial fields and the ability of the model to establish a suitable dynamic balance among different variables through adjustment. In our experiment, the radial velocity data are analyzed by

Observed radial velocity
Scan Time:05/08/2003 22:11

Predicted radial velocity
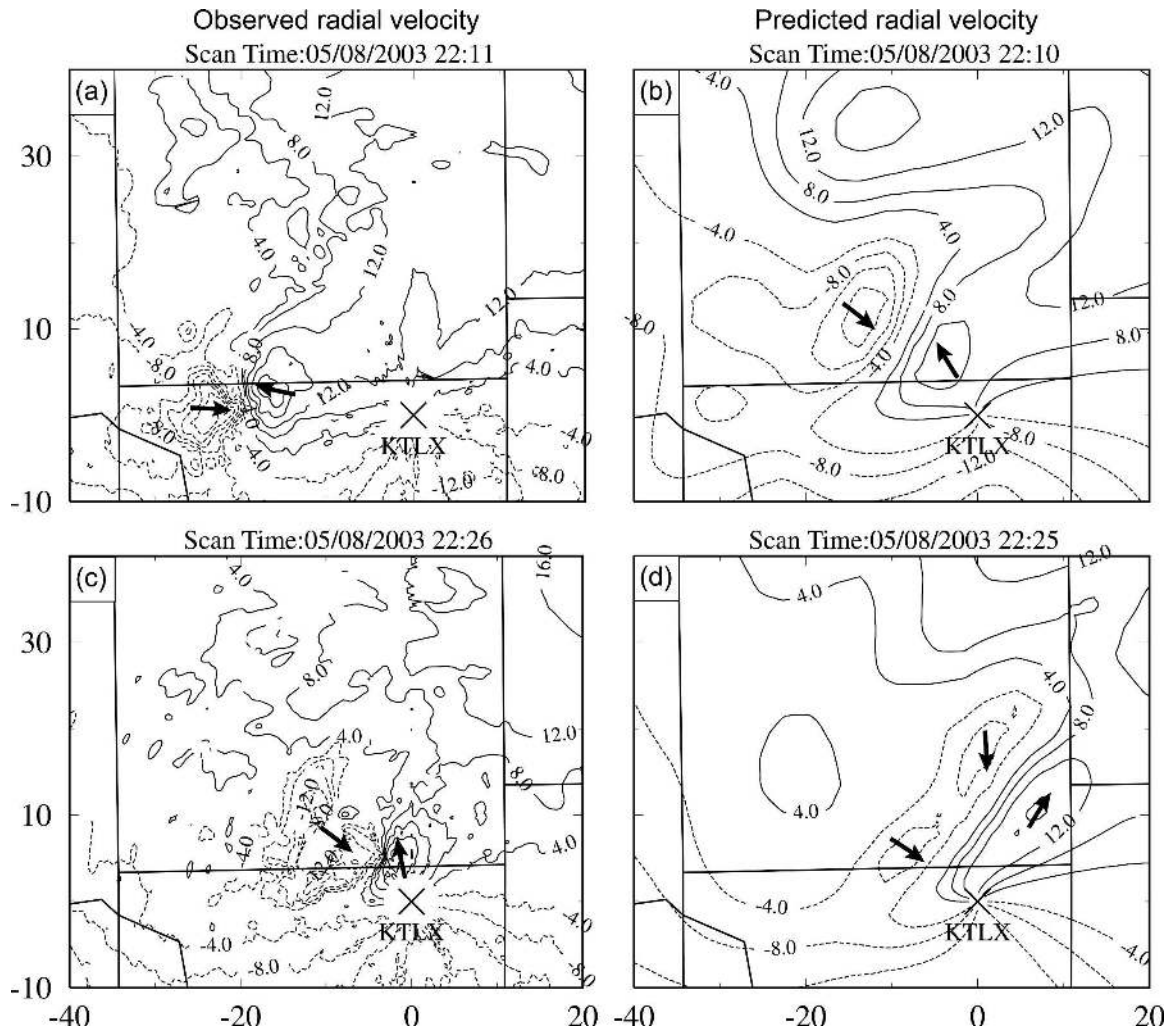### Scan Time:05/08/2003 22:10

FIG. 5. Observed radial velocity fields at the (a), (c) 1.45° elevation of the KTLX radar and (b), (d) corresponding predicted fields from the control experiment at (a), (b) 2210 and (c), (d) 2225 UTC 8 May 2003. The x and y coordinates are in kilometers and originate at the KTLX radar site that is marked by a times sign. The positive radial velocity is contoured as solid lines from 4 to 24 m s^{-1} with 4 m s^{-1} intervals and the negative as dashed lines from -4 to -24 m s^{-1} with the same intervals. The arrows in the figure show the direction of radial velocity in the areas of maximum value.

the ARPS 3DVAR under a mass divergence constraint and the reflectivity data are used through the cloud analysis to adjust in-cloud temperature, moisture, and hydrometeor fields. Apart from the velocity components that are coupled through the mass continuity equation, the other analysis variables are analyzed more or less independently. Therefore, the analysis fields are not consistent with model dynamics and physics in general. Starting from such initial conditions, the model forecast must undergo some adjustments during the initial period to build up a dynamically consistent storm and such adjustments take some time to complete. For this reason, it is desirable that a new analysis is started when a reasonable dynamic consistency has been reached through model adjustment; analysis

cycles that are too short do not necessarily lead to better final analysis. This is, in general, not true for more sophisticated data assimilation techniques, such as the ensemble Kalman filter method, in which flow-dependent background error covariances help produce consistent analyses that allow for high-frequency analysis cycles without degrading the final analysis. Xue et al. (2006) show that with simulated data, radar data at 1-min volume scan intervals produce better analyses than those collected at lower volume scan frequencies.

The maximum vertical velocity (Wmax) can be used as an indicator of the initial adjustment during the model forecast. The maximum vertical velocities for the first 20 min of model forecasts starting from the intermediate analyses of assimilation experiments
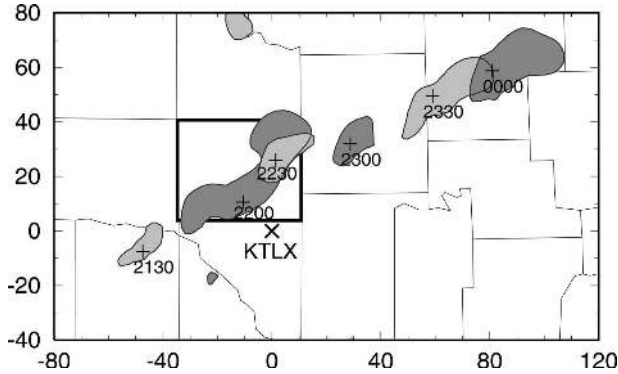
FIG. 6. As in Fig. 3b, but for experiment 5B30E30MA.

5B30E30MA and 10B30E30LH at 0 (2030 UTC, the initial stage), 30 (2100 UTC, the middle stage), and 50 (2120 UTC, the late stage) minutes into the AW are plotted as solid curves in Fig. 8. The dashed curves in Fig. 8a are for the forecasts starting from the analyses one analysis cycle or 5 min later. The curves of Wmax at all three stages show similar shapes in both 5-min and 10-min analysis cycle experiments (Fig. 8). For the forecasts starting from the first analysis over the period from 0 to 20 min, Wmax increases from values below 5 m s^{-1} to maximum values above 33 m s^{-1} in 12–14 min and then drops sharply in the next 6–8 min. For the forecasts starting at 30 min, Wmax values increase from analyzed values between 20 and 25 m s^{-1} to their maximum values close to 40 m s^{-1} in 5–7 min and then drop more slowly. For the forecasts starting at 50 min, Wmax values increase sharply in the first 1–2 min, reach the maximum values slowly in 7–8 min, and then decrease slowly. It is clear that even for the forecasts that start from cycled initial conditions, such as those at 30 and 50 min, the model still needs more than 5 min to establish strong vertical motion and to produce a more dynamically consistent state. Further, Wmax values at 35 and
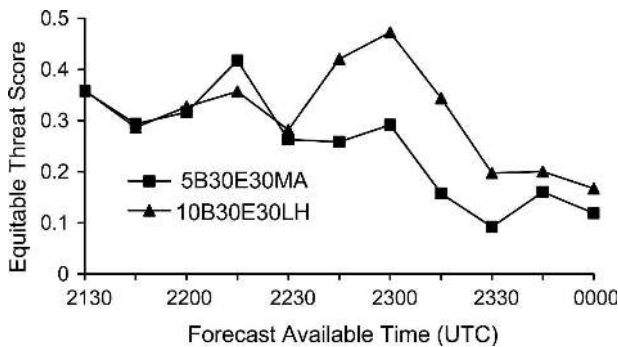

FIG. 7. Equitable threat scores for the predicted 1.45° elevation reflectivity for the 45-dBZ threshold of experiments 5B30E30MA and 10B30E30LH.
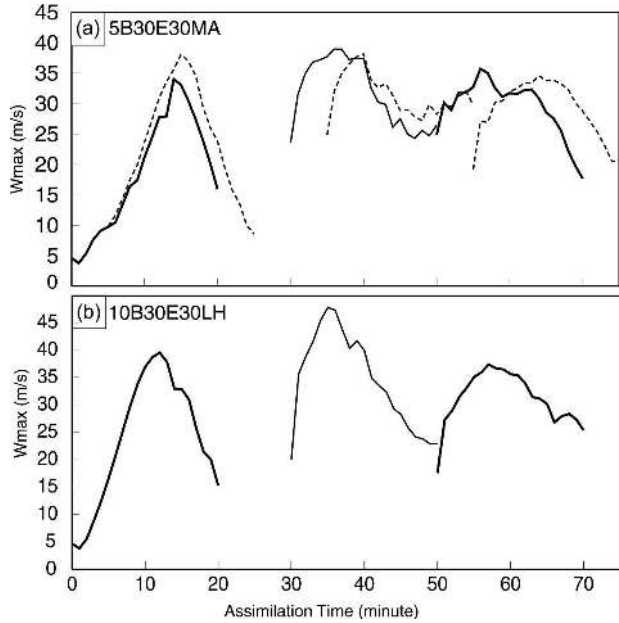

FIG. 8. Maximum vertical velocities for the first 20 min of forecasts starting from the (a) 5B30E30MA analyses and (b) 10B30E30LH analyses at 0 (2030 UTC), 30 (2100 UTC), and 50 (2120 UTC) minutes into the assimilation cycles (solid lines with differing thickness for consecutive times). In (a), a set of forecasts starting from the 5B30E30MA analyses one assimilation cycle later are represented by dashed lines.

55 min in experiment 5B30E30MA (dashed lines in Fig. 8a) are clearly lower than the values from the forecasts starting 5 min earlier. So, when analysis cycles shorter than 10 min are used, the model does not have enough time to spin up the updraft in the model from the new analysis, whose updraft strength tends to be reduced by the analysis step. For these reasons, 10-min analysis cycles work better than 5-min cycles. On the other hand, when the analysis intervals are too long, such as 15 min, the insufficiently spunup storms in the model would have weakened significantly by the time of the next analysis. This explains why 10-min analysis cycles work better than 5- and 15-min cycles (not shown).

c. The impact of in-cloud temperature adjustment schemes

As mentioned earlier, the ARPS cloud analysis has two in-cloud temperature adjustment schemes: the latent heat scheme that calculates the temperature adjustment from the latent heat release corresponding to the added cloud water and ice by the analysis and the moist-adiabat scheme that adjusts in-cloud temperature based on a moist adiabat corresponding to an air parcel lifted from the low level. The effect of entrainment is considered for the latter scheme. The MA scheme is
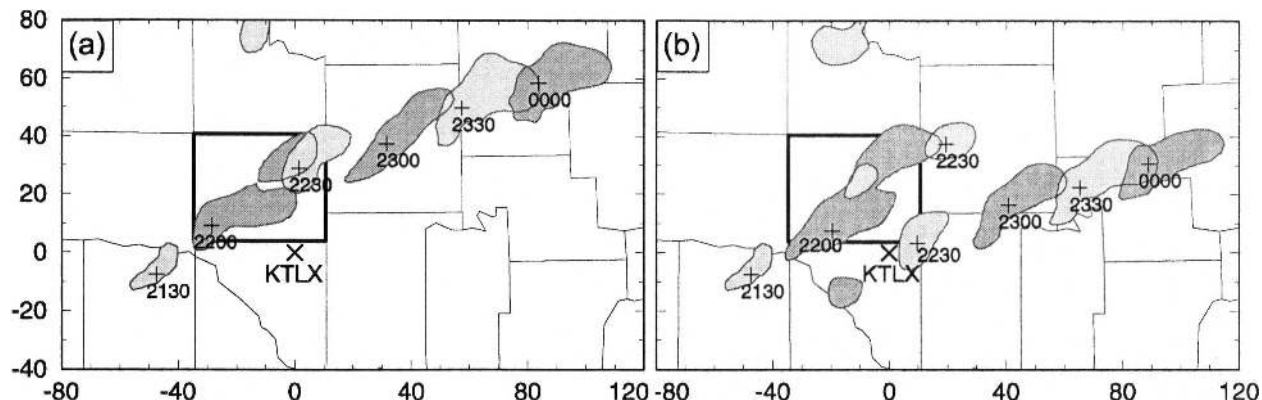
FIG. 9. As in Fig. 3b, but for experiments (a) 10B30E30MA and (b) 5B30E30LH.

more consistent with the physics of a convective storm because it reflects the temperature change in an ascending moist air parcel, while repeated applications of the LH scheme can lead to multiply counting the same latent heating associated with the condensed water or ice because the addition of latent heating in the later analysis cycles does not take into account any heat already added during the earlier analysis cycles.

The temperature adjustment is very important for sustaining existing convection and the use of different schemes can impact the storm forecast significantly (Hu et al. 2006a). To further study the impact of the temperature adjustment schemes and their interaction with the other assimilation parameters, experiments 10B30E30MA and 5B30E30LH are conducted. They are the same as 10B30E30LH and 5B30E30MA, respectively, except for the temperature adjustment scheme used (Table 1). The regions of predicted reflectivity exceeding 45 dBZ at the 1.45° elevation are shown in Fig. 9 for 10B30E30MA and 5B30E30LH. The ETSs of the same reflectivity fields for the 45-dBZ threshold are plotted in Fig. 10. The scores from 5B30E30MA are also included for the convenience of comparison.

Similar to 5B30E30MA, 10B30E30MA predicts the propagation of the OKC storm well but the predicted change in the storm strength is opposite to that observed (Figs. 9a, 6). Compared to 10B30E30LH, the predicted storm in 5B30E30LH dissipates too early. This early dissipation appears to be related to the spurious cell that develops in the model south of the OKC storm and propagates east-northeastward during the last 2 h of forecast (Figs. 9b, 3b).

The ETSs of these four experiments agree with the subjective evaluation (Figs. 10, 7). 10B30E30LH has the highest scores most of the time, especially for forecasts over 1 h; 10B30E30MA has lower scores than 5B30E30MA most of the time because the former over-

predicts the OKC storm even more at those times; 5B30E30LH has zero scores after 1 h because the predicted OKC storm dissipates after 1 h of forecast.

The in-cloud temperature adjustment increases the temperature inside the storm and therefore increases potential energy (or buoyancy) in the system that supports the development of the storm. To quantitatively estimate the effect of temperature adjustment by two different schemes, the total potential energy added to the model atmosphere by the temperature adjustment in all analysis cycles is calculated for the above four experiments and the results are 9.54×10^{16} J in 10B30E30LH, 16.79×10^{16} J in 5B30E30LH, 2.35×10^{16} J in 10B30E30MA, and 4.16×10^{16} J in 5B30E30MA. The LH scheme adds much more, approximately 4 times as much potential energy as the MA scheme for the assimilations with the same number of cycles. Further, the use of more cycles tends to add more energy into the system, and it is more so with the LH scheme by design.

As an important indicator of the vigor of a storm, the vertical velocity fields at 7-km mean sea level (MSL) are shown for 2130 UTC (the end time of the assimila-
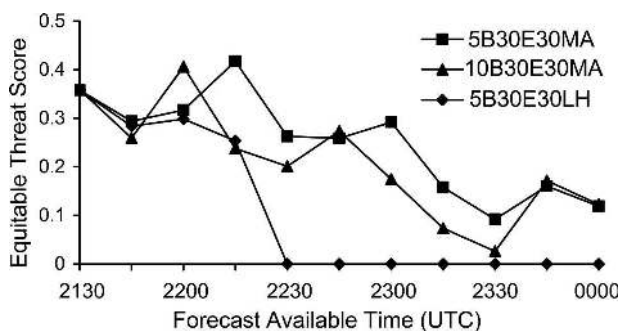

FIG. 10. Equitable threat scores for the predicted 1.45° elevation reflectivity for the 45-dBZ threshold of experiments 5B30E30MA, 5B30E30LH, and 10B30E30MA.
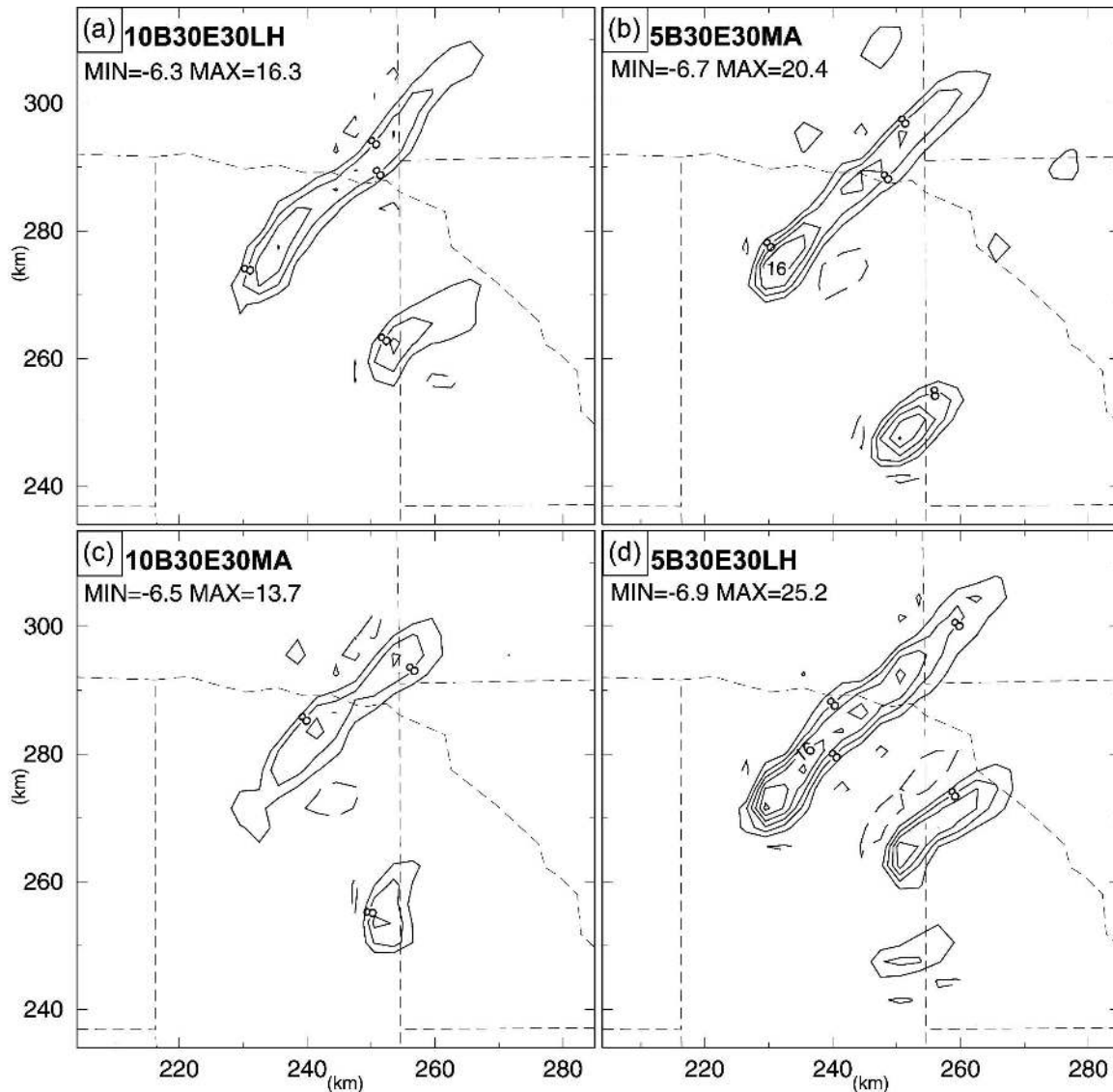
FIG. 11. Vertical velocity fields at 7-km MSL at the end of assimilation (2130 UTC) in experiments (a) 10B30E30LH, (b) 5B30E30MA, (c) 10B30E30MA, and (d) 5B30E30LH. The domain shown represents the portion of 3-km grid between 205 and 285 km in the east–west direction and between 235 and 315 km in the north–south direction. The contour interval is 4 m s^{-1}.

tion) in Fig. 11 for 10B30E30LH, 5B30E30MA, 10B30E30MA, and 5B30E30LH. Two updraft centers, one related to the OKC storm and the other related to storm A (cf. Fig. 2), are found at this time in all four experiments (there is another much weaker updraft in 5B30E30LH). However, their strengths are very different as a result of using the different temperature adjustment schemes and/or different analysis frequencies (Fig. 11). With a higher analysis frequency (5-min intervals) and the LH scheme, 5B30E30LH produces the strongest main updraft of the OKC storm (Fig. 11d) among all four experiments, but the predicted OKC storm dissipates in about 1 h (Fig. 9b). At the same

time, storm A, associated with the strong updraft south of the OKC storm, develops into a strong storm in the forecast instead of dissipating as observed (Fig. 9b). The wrong behaviors of both storms and the extra strength of the updrafts indicate that too much potential energy (16.79 × 10^{16} J) had been added into both storms. Apparently, the overloaded energy causes development too fast and dissipation too early of the OKC storm and the spurious intensification of storm A. The dissipation of the OKC storm might have been caused by the low-level outflow from storm A, located southeast of it in the model. At the opposite end, using a lower frequency (10-min intervals) and the MA

scheme, 10B30E30MA adds only about 1/8 of the potential energy as 5B30E30LH and the resulting updrafts are much weaker and smaller in size (Fig. 11c). Although storm A correctly dissipates quickly in the forecast, the predicted OKC storm strengthens very slowly in the entire 2.5 h of forecast (Fig. 9a), indicating that not enough potential energy has been added into the OKC storm. This slows the development of the OKC storm and delays the start of dissipation of the predicted storm also.

The strength and area coverage of the updrafts of 10B30E30LH and 5B30E30MA are between those of 10B30E30MA and 5B30E30LH. As pointed out earlier, the forecast of 10B30E30LH for the OKC storm is the best among all the experiments, while the forecast of 5B30E30MA for the storm is reasonably good, although neither forecast handles the dissipation of the OKC storm well.

In the above four experiments, the 7-km height updrafts associated with the OKC storm are shown as having an elongated shape extending as long as 50 km; this is not very realistic for a supercell. However, it appears to be consistent with our analysis procedure on which the cloud analysis relies in the current case, mostly in using the observed reflectivity to define the cloud and hydrometeor fields and to adjust in-cloud temperature and moisture (see Hu et al. 2006a,b for more details on the analysis procedure). With the procedure, latent heating is introduced into the regions where reflectivity is observed, although additional conditions such as a minimum vertical velocity have to be met too (Hu et al. 2006a). The shapes of the analyzed updraft associated with the OKC storm are generally in agreement with the shape of the observed radar echoes near this time (see, e.g., the lower-elevation 35-dBZ reflectivity contours at 2131 UTC in Fig. 2). When both radial velocity and reflectivity data are assimilated using more advanced methods, such as the 4DVAR or ensemble Kalman filter methods, the analyzed fields are expected to be more dynamically consistent (see, e.g., Tong and Xue 2005 and discussion therein). We do want to point out here that a maximum updraft center of somewhat circular shape does exist in all cases at or near the southwestern end of the elongated region that is apparently associated with the observed main storm cell. Further, in the forecasts starting from these initial conditions, the updraft generally evolves into a more circular shape near the analyzed maximum center at the southwestern end while the rest of the updraft becomes disorganized. This suggests that through model adjustment, a more dynamically consistent state can be established during the forecast.

The above analyses clearly show that to obtain a good forecast, the right combinations of the in-cloud temperature adjustment scheme and the analysis frequency are necessary given the length of the AW. When the analysis cycles are 10 min long and span over a 1-h AW, the LH scheme outperforms the MA scheme. This is, however, the opposite when 5-min analysis cycles are used; in this case, the MA scheme outperforms the LH scheme. Based on the analyses of the amount of potential energy added into the model by the assimilation procedure and the response of the model atmosphere in terms of storm evolution, it is clear that the right amount of energy input is the key in promoting and sustaining yet not overintensifying observed storms, leading to good forecasts over the life cycle of the storm. Since the LH scheme tends to add more energy into the system than the MA scheme, the use of the LH scheme is generally preferred when analysis frequency is low (e.g., 10 min) while the MA scheme is usually preferred when using, for instance, a 5-min frequency. For this reason, most of the additional experiments to be examined next use the combinations of a 5-min interval and MA scheme or a 10-min interval and LH scheme (see Table 1).

d. The impact of the length and temporal coverage of the assimilation window

In the earlier experiments, the assimilations start about 10 min before the OKC storm initiation and cover the entire development stage of the storm. Here, eight additional experiments classified into two groups are conducted to study the impact of different lengths and coverage of the AW (Table 1). For the first group of experiments, including 10B30E10LH, 10B30E20LH, 5B30E10MA, and 5B30E20MA, the assimilation starts at 2030 UTC (the same as the earlier four experiments) but ends at 2110 or 2120 UTC. The second group includes 10B40E30LH, 10B60E30LH, 5B40E30MA, and 5B60E30MA and their AWs all end at 2130 UTC but start at 2040 or 2100 UTC. Both 5- and 10-min assimilation frequencies are tested in these two groups. For brevity, we only show the summary reflectivity plots. Those for the first group of experiments are shown in Fig. 12 and those for the second group are in Fig. 13.

As stated in the case introduction, the first echo of the OKC storm appeared at about 2040 UTC and the echo exceeded 35 dBZ by 2101 UTC. From then on, the OKC storm grew quickly and developed into a strong supercell by 2131 UTC (cf. Fig. 2). The AWs of the first group of experiments mainly cover the early part of the development stage (from 2040 to 2110 UTC) of the OKC storm. In 10B30E10LH and 5B30E10MA, the first 30 min of storm life (2040–2110 UTC) are covered by the 40-min AWs (2030–2110 UTC). The predicted
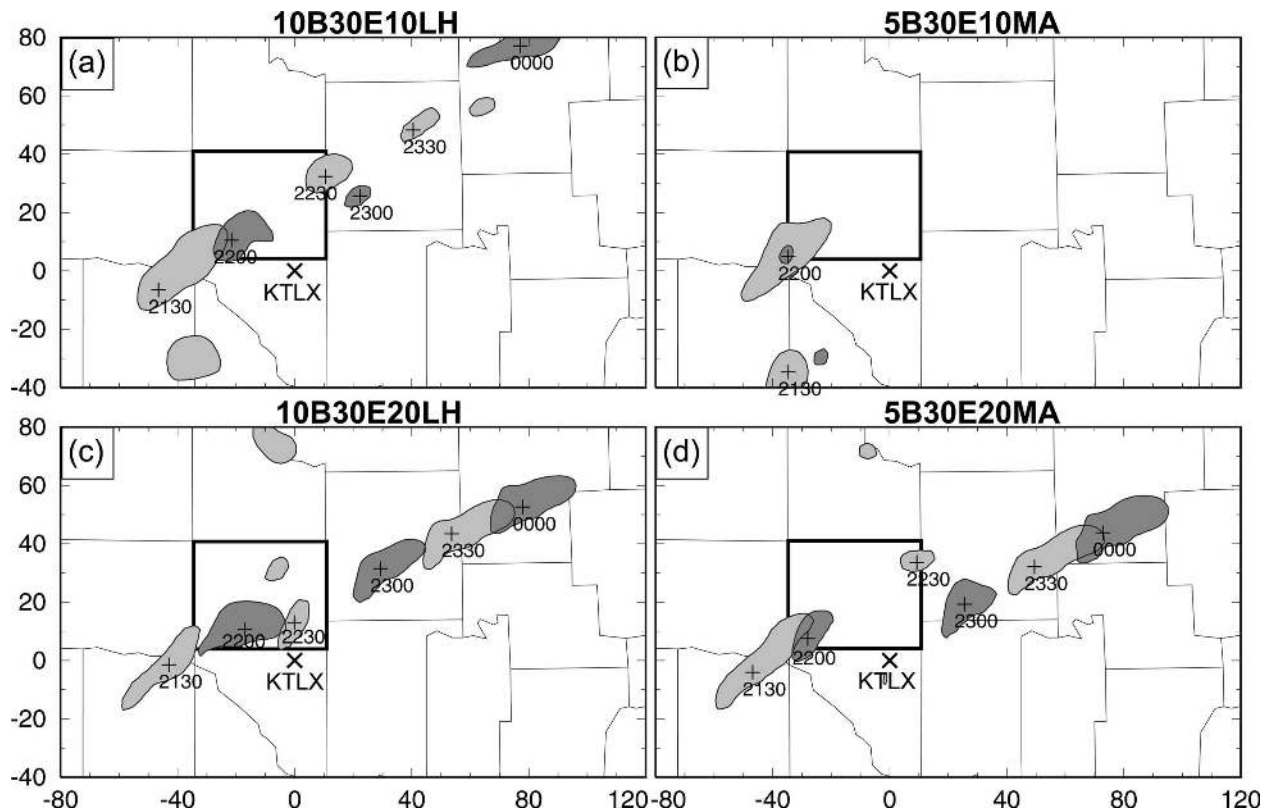
FIG. 12. As in Fig. 3b, but for experiments (a) 10B30E10LH, (b) 5B30E10MA, (c) 10B30E20LH, and (d) 5B30E20MA.

storm in 5B30E10MA disappears completely after 2200 UTC, or 50 min into the forecast (Fig. 12b), while that in 10B30E10LH lasts until 2230 UTC (80 min into the forecast) and has correct maximum echo locations at 2130 and 2200 UTC (Fig. 12a). A spurious cell develops in 10B30E10LH southeast of the OKC storm, however, and is visible from 2300 UTC on. Obviously, the OKC storm was not fully built up by the assimilation, and the spurious storm developing to its southeast probably had a negative impact too.

When the AW is extended by 10 min in 10B30E20LH and 5B30E20MA to 2120 UTC, now including more radar observations, the forecast is improved for each. The predicted OKC storm in 5B30E20MA lasts until 2230 UTC and has better positioning at 2130 and 2200 UTC (Fig. 12d). Similar to the 10B30E10LH, a spurious cell also develops in the model and has become stronger than the OKC storm by 2300 UTC. The OKC storm dissipates later while this spurious storm becomes stronger. The forecast of 10B30E20LH is much better than that of 10B30E10LH and appears close to the best forecast, that of 10B30E30LH (Figs. 12a,c, 3b). A more detailed look at the forecast reflectivity fields every 5 min between 2200 and 2230 UTC indicates that the predicted OKC storm actually dissipates quickly after

2200 UTC, while a new storm quickly develops in its place and propagates along the path of the observed OKC storm in the rest of the forecast.

The AWs of the second group of experiments mainly cover the later development stage (from 2100 to 2130 UTC) of the OKC storm. Although the AWs from 2040 to 2130 UTC of 10B40E30LH and 5B40E30MA include all radar observations used in 10B30E30LH and 5B30E30MA, the forecasts of the former are worse than those of the latter (Figs. 13a,b, 3, 6), mainly because of larger northwestward displacement errors at the later forecast time. These results indicate that even though the first 10 min of the 3-km assimilation precede the initiation of the OKC storm and therefore the availability of radar data, the additional period of AW is still beneficial. The spinning up of the 9-km solution at 2030 UTC on the 3-km grid to arrive at a better forecast background for the 3-km analysis at 2040 UTC must be the reason. When the AW is started even later, at 2100 UTC, and includes only the later part of the development stage of the OKC storm, the predicted paths of the OKC storm in 10B60E30LH and 5B60E30MA deviate northward even more (Figs. 13c,d).

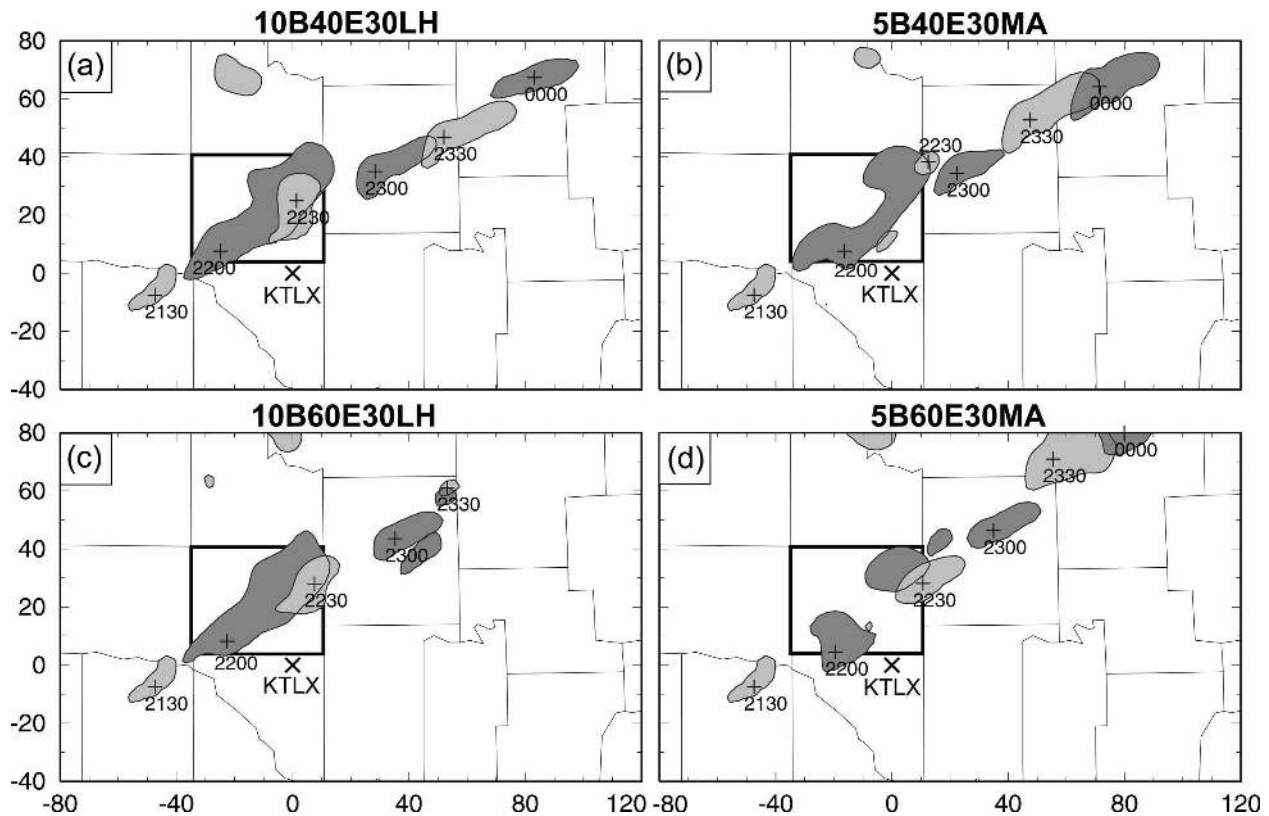The results of the two groups of experiments and those from 10B30E30LH and 5B30E30MA clearly sug-

FIG. 13. As in Fig. 3b, but for experiments (a) 10B40E30LH, (b) 5B40E30MA, (c) 10B60E30LH, and (d) 5B60E30MA.

gest that an AW of about 1-h long, covering the entire developmental stage of the OKC storm as well as a prestorm period, is necessary in this case to obtain a good analysis and subsequent forecast of the storm. When the AW is relatively short, covering the later part of the developing stage is more effective in building a sustainable storm in the model.

e. Comparison of initial fields

To further understand the impact of assimilation configurations, the initial fields of 5B30E10MA (in which the OKC storm dissipates in the first hour of the forecast) and 5B30E30MA (which captures well the propagation of the storm as a strong cell throughout the 2.5 h of the forecast) are plotted in Fig. 14. With a 20-min-longer assimilation window that covers the later stage of the storm initiation, the updraft and the associated positive temperature perturbations in the initial fields of 5B30E30MA are much stronger than those in 5B30E10MA (Figs. 14a–d). Comparing the vertical velocity at 7-km MSL of the above two experiments (Figs. 14e,f), 5B30E30MA with a 20-min longer AW has a stronger OKC storm but a slightly weaker storm A in its initial condition, consistent with the intensification

of the OKC storm and the weakening of storm A during this 20-min period. This suggests that during this period the data assimilation correctly strengthened the OKC storm, resulting in a more sustainable storm. It also reduced the intensity of storm A and its otherwise negative impact on the evolution of the main OKC storm. It appears that at the end of the AW of 5B30E10MA, the OKC storm has not been fully built up to be sustainable in the subsequent forecast.

Because of the lack of a more reliable analysis of the storms at the initial condition times, it is not easy to tell exactly which initial condition is better than the others. Some of the analyses above attempt to gauge the quality of the initial conditions based on their physical realism and their agreement with our conceptual understanding of the storms, but their value is limited. In this paper, we choose to rely mainly on the quality of the subsequent forecast to determine the proper choice of assimilation configuration, which is also our main goal.

f. Results of experiment 5B60E30LH

It is found earlier that experiment 5B60E30MA, which uses 5-min analysis cycles over a 30-min AW and the MA scheme, initializes the OKC storm that dissi-
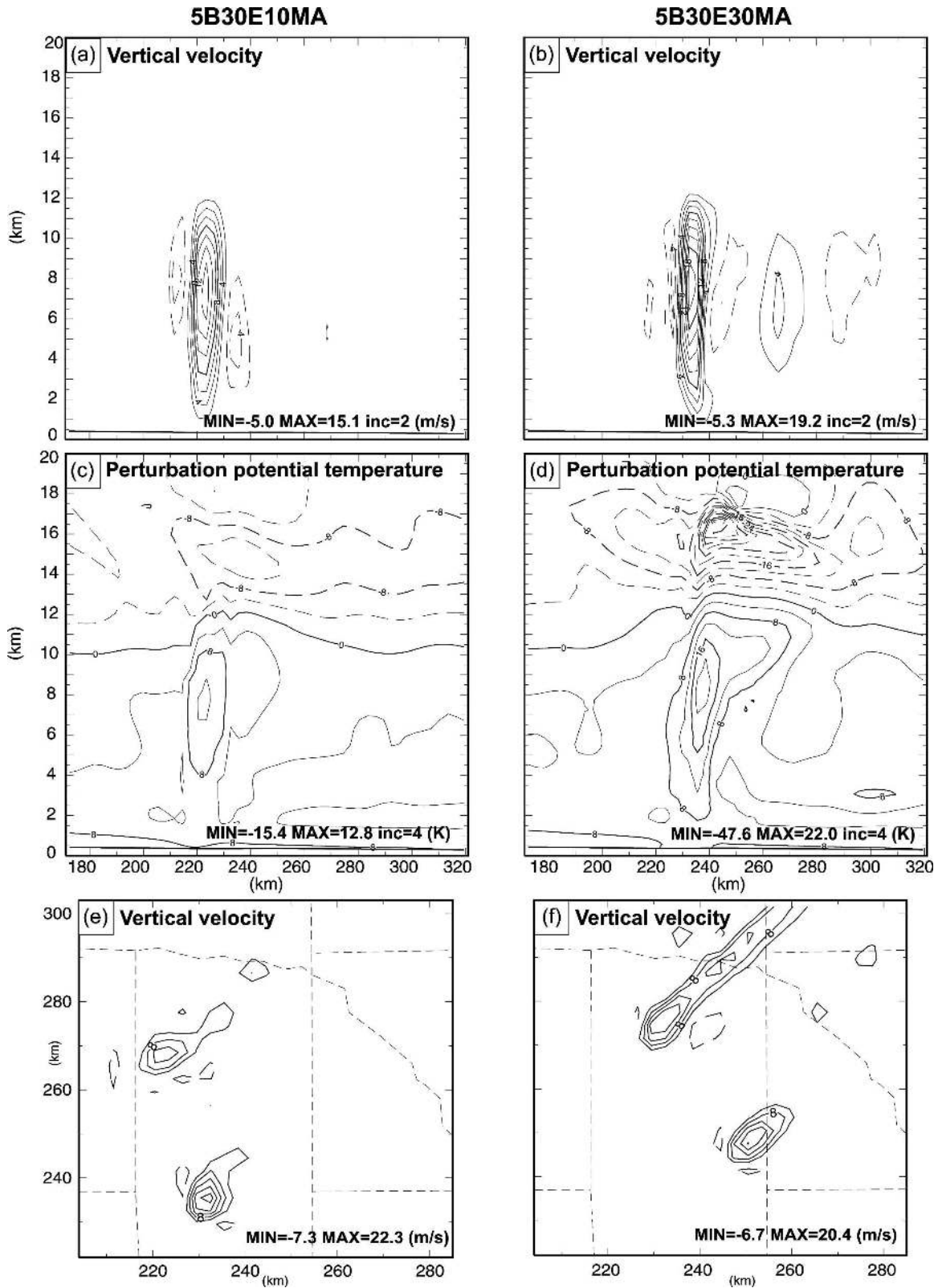
FIG. 14. The initial fields of experiments (a), (c), (e) 5B30E10MA and (b), (d), (f) 5B30E30MA. Here, (a) and (b) are the *x–z* cross sections of vertical velocity fields through the maximum vertical velocity area of the OKC storm, (c) and (d) are the corresponding cross sections of perturbation potential temperature, and (e) and (f) are the vertical velocity fields at 7-km MSL.

pates quickly (Fig. 13d). Another storm that develops to the southeast of the OKC storm maintains its intensity but propagates too far north. Experiment 5B30E30LH, which uses a 1-h AW with 5-min intervals and the LH scheme, produces a storm that develops too fast (Fig. 9b), apparently due to too much potential energy added by the LH scheme. Based on these observations, a new experiment (5B60E30LH) is performed, which is the same as 5B60E30MA except for the LH scheme used. The question to ask is when the assimilation window is short, can the extra potential energy afforded by the LH scheme help sustain the initialized storm?

The results of 5B60E30LH are shown in Fig. 15. Compared to 5B60E30MA, 5B30E30LH, and the observations (Figs. 15, 13d, 9b, 3a), 5B60E30LH captures the general evolution and propagation of the OKC storm rather well, and the storm remains a strong supercell up to the end of the 2.5 h of forecast. The significant improvement in the forecast of 5B60E30LH, when compared to 5B60E30MA, reflects the importance of a proper combination of assimilation parameters, especially when certain parameters (such as the AW length) are constrained by practical limitations (such as those found with real-time applications). In the case of 5B60E30LH, the insufficient AW length can be compensated for by using a temperature adjustment scheme that adds more energy into the system than can otherwise be justified. In real-time applications where the truth is unknown and data and computational constraints exist, the careful consideration and setup of the assimilation systems according to the findings of experiments like ours are necessary, at least when using similar methods as used here. The AW length will be less of an issue, however, if high-frequency assimilation cycles are run continuously, similar to the way typical operational NWP systems do, except that much shorter assimilation cycles are used here.

5. Summary and further discussion

In this paper, the ARPS 3DVAR and cloud analysis procedures are successfully applied to the analysis and prediction of the 8 May 2003 Oklahoma City tornadic thunderstorm case using an intermittent procedure that assimilates the scan volumes of the Oklahoma City WSR-88D radar (KTLX) with proper assimilation configurations.

A 3-km grid nested within a 9-km grid is used for both assimilation and forecasting. The model storm in the 3-km grid is established through the intermittent assimilation cycles. For each 3-km analysis, the 3DVAR is used to analyze conventional observations
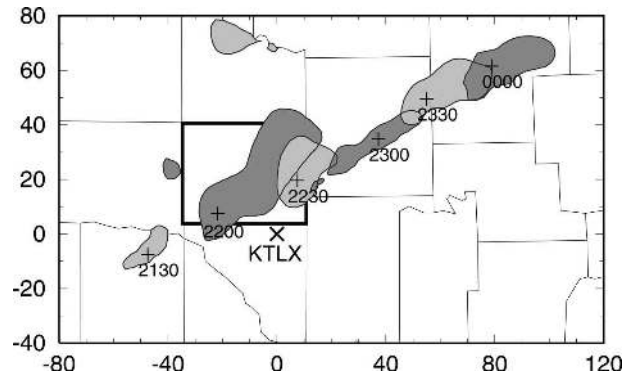

FIG. 15. As in Fig. 3b, but for experiment 5B60E30LH.

and the radial velocity data in a similar way to that of Hu et al. (2006a), and the cloud analysis is performed to analyze the reflectivity data. Forecasts for up to 2.5 h are performed starting from the assimilated initial conditions, and their quality is used to evaluate the performance of assimilation.

A total of thirteen 3-km experiments with different assimilation configurations are conducted to study the impact of the analysis frequency, in-cloud temperature adjustment scheme, and lengths and coverage of the assimilation window (AW) on the final analysis and forecast.

The best forecast for the OKC storm comes from the experiment that uses a 1-h-long AW with 10-min analysis cycles and an in-cloud temperature adjustment scheme that is based on latent heat release related to the input of cloud condensate (the LH scheme). The experiment predicts the propagation of the OKC storm with position errors of less than 8 km throughout the 2.5 h of forecast in terms of the maximum reflectivity center of the main storm. The supercell characteristics of the storm during the forecast are also captured even though the grid spacing of the experiment is a relatively coarse 3 km for the purpose of resolving the tornado vortex or even the mesocyclone. The predicted mid- and low-level fields show a column of strong vorticity associated with the predicted OKC storm during the entire forecast.

It is interesting to note here that a preliminary study by Wicker and Dowell (2004) performed an assimilation and prediction study on this same case with the ensemble Kalman filter method at 1-km horizontal resolution. The radar reflectivity field at the end of assimilation looks very close to the observed one, and the wind fields appear dynamically consistent too, probably more so than the analyzed fields in our experiments. Unfortunately, the predicted storm in the case does not last beyond 40 min of the forecast. Apart

from the assimilation methods used, another significant difference between our study and their study lies in the fact that a single sounding is used to define the storm environment in their case; the representativeness of this time-invariant environment may be a cause of the less successful prediction. For example, the CAPE in the model soundings extracted from the 3-km control simulation 10B30E30LH at the Norman, Oklahoma (OUN), site changes from 2888 J kg^{-1} at 2130 8 May to about 5000 J kg^{-1} at 0000 9 May. Furthermore, our experiments employ a full physics package rather than cloud physics only.

When the higher assimilation frequency (i.e., once every 5 min) is used with a 1-h AW and the moist-adiabat (MA) scheme (in 5B30E30MA), the forecast is reasonably good, though slightly worse than the control experiment (10B30E30LH) with 10-min intervals and the LH scheme even though more radar observations are assimilated in the former. This behavior is partly related to the fact that the model almost always requires more than 5 min to complete the initial adjustments, and a 10-min analysis interval is needed to give the model enough time to establish dynamica consistency among the model variables and to build a sustainable storm. Among all configurations considered, 5B30E30MA is theoretically the best because all radar scan volumes within an AW that covers the entire development period of the main storm are used together with the MA scheme that is based on a simple cloud physics model and is less sensitive to the number of cycles applied because it only makes the adjustment necessary to fit a diluted moist adiabat (Brewster 2002; Hu et al. 2006a).

The study of two in-cloud temperature adjustment schemes available in the ARPS cloud analysis procedure shows that the total potential energy added into storms by assimilation can significantly impact the storm forecast. A combination of 10-min analysis intervals with the LH scheme or 5-min intervals with the MA scheme is found to work the best for 1-h-long AWs. But we also found that the former combination is better than the latter because the model needs more than 5 min to complete the initial adjustment, as explained in detail earlier. Our previous study (Hu et al. 2006a,b) with a similar assimilation system also shows similarly important impacts of in-cloud temperature adjustment on the storm forecast and furthermore finds that the use of radial velocity along with reflectivity does incrementally improve the storm forecast.

The experiments testing the impact of the lengths and coverage of the AW are also interesting. It is found that taking only 10 min out of the 1-h-long AW either at the beginning or the end can significantly reduce the forecast quality of the main storm, and in general, the shorter the AW, the worse the forecast. With a short AW, applying the AW at the later part of the development stage of the storm is more effective than that applied at the early part. In practice, it is desirable to use an AW that is as short as possible in order to have a forecast lead time that is as long as possible, and in this case, a long lead time for forecasting the storm behaviors at the tornado outbreak. Our experiments also indicate that an AW of at least 30 min is necessary. In our 28 March 2000 downtown Fort Worth tornadic thunderstorm case (Hu et al. 2006a,b), a lead time of over 1 h is achieved for the prediction of strong low-level rotation that appears to be closely linked to the observed tornadogenesis.

The analysis of the initial fields from experiments 5B30E30MA and 5B30E10MA suggests that the additional 20-min assimilation period of 5B30E30MA during the later stage of the OKC storm initiation correctly strengthens the OKC storm and reduces the negative impact of storm A. Because of the lack of a more reliable analysis of the storms at the initial condition time and the high nonlinearity of the storm system during the forecast, however, a complete understanding of the improvement of individual aspects in the initial conditions is not easy. Thorough sensitivity analyses, using approaches such as that of Martin and Xue (2006), may be necessary.

To see what we can do with a 30-min AW located at the later stage of storm development, experiment 5B60E30MA is repeated using the LH scheme in 5B60E30LH. The reduced AW length is compensated for by the extra potential energy input provided by the LH scheme, resulting in a reasonably well-developed storm by the end of the AW. Such results are also consistent with the analysis on temperature adjustment by Hu et al. (2006a).

The above conclusions are mainly based on the 8 May 2003 Oklahoma City tornadic storm case, although some have also been drawn from our earlier study on the Fort Worth tornadic thunderstorm case. The quantitative aspects may also be tied to the specific analysis schemes used, that is, the ARPS 3DVAR and cloud analysis. A general conclusion is that the assimilation configurations can significantly impact the results of radar data assimilation and subsequent storm forecasting. The configurations should be carefully evaluated and tested, in a similar but perhaps even more thorough way than is done here. When continuous assimilation cycles are used, the optimal AW length is less of an issue for a given scheme. The experiments on AW coverage provide us with some guidance on the design of post-real-time assimilation experiments, and for real-

time applications, provide some guidance on the results we can expect.

Even though theoretically less than optimal, the current intermittent assimilation procedure for incorporating full-volume Doppler radar data into a storm prediction model is computationally inexpensive and operationally feasible. For real-time operational applications, the computation efficiency of a configuration may carry more weight. When similar forecast qualities are obtained, an assimilation configuration that requires the least amount of data processing and computation and provides the longest forecast lead time for the features that we are most interested in is obviously preferred, and such a configuration may be the one of choice even if the resultant prediction is slightly worse. In the future, similar issues for other types of convective systems, such as the less-persistent multicellular storms and the larger-scale squall lines and mesoscale convective complexes, should also be investigated.

REFERENCES

Albers, S. C., J. A. McGinley, D. A. Birkenheuer, and J. R. Smart, 1996: The local analysis and prediction system (LAPS): Analysis of clouds, precipitation and temperature. *Wea. Forecasting,* **11,** 273–287.

Bratseth, A. M., 1986: Statistical interpolation by means of successive corrections. *Tellus,* **38A,** 439–447.

Brewster, K., 1996: Application of a Bratseth analysis scheme including Doppler radar data. Preprints, *15th Conf. on Weather Analysis and Forecasting,* Norfolk, VA, Amer. Meteor. Soc., 92–95.

——, 2002: Recent advances in diabatic initialization of a non-hydrostatic numerical model. Preprints, *15th Conf. on Numerical Weather Prediction/21st Conf. on Severe Local Storms,* San Antonio, TX, Amer. Meteor. Soc., CD-ROM, J6.3.

Brock, F. V., K. C. Crawford, R. L. Elliott, G. W. Cuperus, S. J. Stadler, H. L. Johnson, and M. D. Eilts, 1995: The Oklahoma Mesonet: A technical overview. *J. Atmos. Oceanic Technol.,* **12,** 5–19.

Crum, T. D., and R. L. Alberty, 1993: The WSR-88D and the WSR-88D operational support facility. *Bull. Amer. Meteor. Soc.,* **74,** 1669–1687.

Daley, R., 1991: *Atmospheric Data Analysis.* Cambridge University Press, 457 pp.

Gal-Chen, T., 1978: A method for the initialization of the anelastic equations: Implications for matching models with observations. *Mon. Wea. Rev.,* **106,** 587–606.

Gao, J., M. Xue, A. Shapiro, Q. Xu, and K. K. Droegemeier, 2001: Three-dimensional simple adjoint velocity retrievals from single-Doppler radar. *J. Atmos. Oceanic Technol.,* **18,** 26–38.

——, ——, K. Brewster, F. Carr, and K. K. Droegemeier, 2002: New development of a 3DVAR system for a nonhydrostatic NWP model. Preprints, *15th Conf. on Numerical Weather Prediction/19th Conf. on Weather Analysis and Forecasting,* San Antonio, TX, Amer. Meteor. Soc., 339–341.

——, ——, ——, and K. K. Droegemeier, 2004: A three-dimensional variational data analysis method with recursive filter for Doppler radars. *J. Atmos. Oceanic Technol.,* **21,** 457–469.

Hu, M., M. Xue, and K. Brewster, 2006a: 3DVAR and cloud analysis with WSR-88D level-II data for the prediction of Fort Worth tornadic thunderstorms. Part I: Cloud analysis and its impact. *Mon. Wea. Rev.,* **134,** 675–698.

——, ——, J. Gao, and K. Brewster, 2006b: 3DVAR and cloud analysis with WSR-88D level-II data for the prediction of Fort Worth tornadic thunderstorms. Part II: Impact of radial velocity analysis via 3DVAR. *Mon. Wea. Rev.,* **134,** 699–721.

Martin, W. J., and M. Xue, 2006: Initial condition sensitivity analysis of a mesoscale forecast using very-large ensembles. *Mon. Wea. Rev.,* **134,** 192–207.

Qiu, C.-J., and Q. Xu, 1992: A simple adjoint method of wind analysis for single-Doppler data. *J. Atmos. Oceanic Technol.,* **9,** 588–598.

——, and ——, 1994: A spectral simple adjoint method for retrieving low-altitude winds from single-Doppler data. *J. Atmos. Oceanic Technol.,* **11,** 927–936.

Schaefer, J. T., 1990: The critical success index as an indicator of warning skill. *Wea. Forecasting,* **5,** 570–575.

Serafin, R. J., and J. W. Wilson, 2000: Operational weather radar in the United States: Progress and opportunity. *Bull. Amer. Meteor. Soc.,* **81,** 501–518.

Shapiro, A., S. Ellis, and J. Shaw, 1995: Single-Doppler radar retrievals with Phoenix II data: Clear air and microburst wind retrievals in the planetary boundary layer. *J. Atmos. Sci.,* **52,** 1265–1287.

Snyder, C., and F. Zhang, 2003: Assimilation of simulated Doppler radar observations with an ensemble Kalman filter. *Mon. Wea. Rev.,* **131,** 1663–1677.

Sun, J., 2005: Initialization and numerical forecasting of a supercell storm observed during STEPS. *Mon. Wea. Rev.,* **133,** 793–813.

——, and N. A. Crook, 1997: Dynamical and microphysical retrieval from Doppler radar observations using a cloud model and its adjoint. Part I: Model development and simulated data experiments. *J. Atmos. Sci.,* **54,** 1642–1661.

——, and ——, 1998: Dynamical and microphysical retrieval from Doppler radar observations using a cloud model and its adjoint. Part II: Retrieval experiments of an observed florida convective storm. *J. Atmos. Sci.,* **55,** 835–852.

——, D. W. Flicker, and D. K. Lilly, 1991: Recovery of three-dimensional wind and temperature fields from simulated single-Doppler radar data. *J. Atmos. Sci.,* **48,** 876–890.

Tong, M., and M. Xue, 2005: Ensemble Kalman filter assimilation

of Doppler radar data with a compressible nonhydrostatic model: OSS experiments. *Mon. Wea. Rev.,* **133,** 1789–1807.

Weygandt, S. S., A. Shapiro, and K. K. Droegemeier, 2002a: Retrieval of model initial fields from single-Doppler observations of a supercell thunderstorm. Part I: Single-doppler velocity retrieval. *Mon. Wea. Rev.,* **130,** 433–453.

——, ——, and ——, 2002b: Retrieval of model initial fields from single-doppler observations of a supercell thunderstorm. Part II: Thermodynamic retrieval and numerical prediction. *Mon. Wea. Rev.,* **130,** 454–476.

Wicker, L. J., and D. C. Dowell, 2004: High-resolution analyses of the 8 May 2003 Oklahoma City storm. Part III: An ultra-high resolution forecast experiment. Preprints, *22d Conf. on Severe Local Storms,* Hyannis, MA, Amer. Meteor. Soc., CD-ROM, 12.6.

Xu, Q., C. Qiu, and J. Yu, 1994: Adjoint-method retrievals of low-altitude wind fields from single-Doppler reflectivity measured during Phoenix II. *J. Atmos. Oceanic Technol.,* **11,** 275–288.

Xue, M., K. K. Droegemeier, V. Wong, A. Shapiro, and K. Brewster, 1995: ARPS version 4.0 user's guide. Center for Analysis and Prediction of Storms, 380 pp. [Available online at http://www.caps.ou.edu/ARPS.]

——, ——, and ——, 2000: The Advanced Regional Prediction System (ARPS)—A multiscale nonhydrostatic atmospheric simulation and prediction tool. Part I: Model dynamics and verification. *Meteor. Atmos. Phys.,* **75,** 161–193.

——, and Coauthors, 2001: The Advanced Regional Prediction System (ARPS)—A multiscale nonhydrostatic atmospheric simulation and prediction tool. Part II: Model physics and applications. *Meteor. Atmos. Phys.,* **76,** 143–166.

——, M. Tong, and K. K. Droegemeier, 2006: An OSSE framework based on the ensemble square root Kalman filter for evaluating the impact of data from radar networks on thunderstorm analysis and forecast. *J. Atmos. Oceanic Technol.,* **23,** 46–66.

Zhang, F., C. Snyder, and J. Sun, 2004: Impacts of initial estimate and observations on the convective-scale data assimilation with an ensemble Kalman filter. *Mon. Wea. Rev.,* **132,** 1238–1253.

Zhang, J., 1999: Moisture and diabatic initialization based on radar and satellite observation. Ph.D. dissertation, School of Meteorology, University of Oklahoma, 194 pp.

——, F. Carr, and K. Brewster, 1998: ADAS cloud analysis. Preprints, *12th Conf. on Numerical Weather Prediction,* Phoenix, AZ, Amer. Meteor. Soc., 185–188.